

A Sensitivity and Array-Configuration Study for Measuring the Power Spectrum of 21cm Emission from Reionization

Aaron Parsons¹, Jonathan Pober¹, Matthew McQuinn¹, Daniel Jacobs², and James Aguirre²

ABSTRACT

Telescopes aiming to measure 21cm emission from the Epoch of Reionization must toe a careful line, balancing the need for raw sensitivity against the stringent calibration requirements for removing bright foregrounds. It is unclear what the optimal design is for achieving both of these goals. Via a pedagogical derivation of an interferometer's response to the power spectrum of 21cm reionization fluctuations, we show that even under optimistic scenarios, first-generation arrays will yield low-SNR detections, and that different compact array configurations can substantially alter sensitivity. We explore the sensitivity gains of array configurations that yield high redundancy in the uv -plane – configurations that have been largely ignored since the advent of self-calibration for high-dynamic-range imaging. We first introduce a mathematical framework to generate optimal minimum-redundancy configurations for imaging. We contrast the sensitivity of such configurations with high-redundancy configurations, finding that high-redundancy configurations can improve power-spectrum sensitivity by more than an order of magnitude. We explore how high-redundancy array configurations can be tuned to various angular scales, enabling array sensitivity to be directed away from regions of the uv -plane (such as the origin) where foregrounds are brighter and where instrumental systematics are more problematic. We demonstrate that a 132-antenna deployment of the Precision Array for Probing the Epoch of Reionization (PAPER) observing for 120 days in a high-redundancy configuration will, under ideal conditions, have the requisite sensitivity to detect the power spectrum of the 21cm signal from reionization at a 3σ level at $k < 0.25h \text{ Mpc}^{-1}$ in a bin of $\Delta \ln k = 1$. We discuss the tradeoffs of low- versus high-redundancy configurations.

Subject headings: cosmology: observations, instrumentation: interferometers, techniques: interferometric, telescopes

1. Introduction

The Epoch of Reionization (EoR) — the rapid ionization of the majority of the hydrogen in the universe by light from the first stars and black holes — is the most recent phase transition in

¹University of California, Berkeley

²University of Pennsylvania

the state of the baryons in our universe, and yet it still remains largely unexplored. Observations of redshifted emission from the 21cm hyperfine transition of neutral hydrogen have the potential to provide unrivaled detail about this epoch (Field 1958; Madau et al. 1997; Furlanetto et al. 2006). Variations in this signal versus redshift and direction allow the reconstruction of a three-dimensional map of the evolution of the ionization state of the hydrogen. However, reaching the sensitivity to image the structures during reionization will require an instrument with roughly a square kilometer of collecting area (McQuinn et al. 2006). As a result, first-generation radio telescopes targeting reionization either aim to measure the global temperature change of 21cm emission during EoR (a task which is not sensitivity-limited), as with the Compact Reionization Experiment (CoRE) and the Experiment to Detect the Global EoR Signature (EDGES; Bowman & Rogers 2010), or instead aim for a statistical detection of the 21cm fluctuations generated by reionization, as with the Giant Metre-wave Radio Telescope (GMRT; Pen et al. 2009)¹, the LOw Frequency ARray (LOFAR; Rottgering et al. 2006)², the Murchison Widefield Array (MWA; Lonsdale et al. 2009)³, and the Donald C. Backer Precision Array for Probing the Epoch of Reionization (PAPER; Parsons et al. 2010)⁴. A detection of the EoR by the first generation of instruments would establish low-frequency radio astronomy as a powerful probe of reionization and of the high-redshift universe.

Removing foregrounds that are orders of magnitude brighter than the signal and obtaining the requisite sensitivity are the primary concerns that influence the design of all 21cm instruments (Parsons et al. 2010; Bowman et al. 2009; Paciga et al. 2010). Astrophysical foregrounds that interfere with the direct detection of a 21cm EoR signature arise primarily from galactic and extragalactic synchrotron and free-free emission. With the exception of leakage terms from Faraday rotated polarized galactic synchrotron emission (Jelić et al. 2008; Bernardi et al. 2010), all contaminants arising from foregrounds are thought to be spectrally smooth or faint enough not to be problematic (Petrovic & Oh 2010). The brightness temperatures of these foregrounds can exceed the expected ~ 10 mK amplitude of the 21cm EoR signal by up to five orders of magnitude (Zahn et al. 2007; Santos et al. 2005). These foregrounds also serve as a source of noise that dominates the system temperature of radiometers in the 100 – 200 MHz band.

Projects aiming to detect the 21cm EoR signal have taken a variety of different approaches, illustrating the breadth of parameter space available for designing such instruments. Much of our discussion will focus on the PAPER experiment, but our results generalize to other arrays. PAPER employs single-dipole antenna elements that are not steerable — a design that emphasizes spatially and spectrally smooth instrumental responses to facilitate calibration and foreground removal (Parsons et al. 2010). This approach contrasts with the large-dish approach taken by GMRT and the station beam-forming approach taken by LOFAR and the MWA, where dipoles are

¹<http://gmrt.ncra.tifr.res.in/>

²<http://www.lofar.org/>

³<http://www.mwatelescope.org/>

⁴<http://eor.berkeley.edu/>

added in-phase to form more focused beams prior to correlation. PAPER’s design choice favors elements with a single primary lobe of response horizon-to-horizon — a choice which directly limits the collecting area of each element. On the one hand, for a fixed total collecting area, small antenna elements (such as PAPER’s) increase the cost of correlation and imaging, owing to the $\mathcal{O}(N^2)$ scaling of the number of baselines with number of antennas N . On the other hand, it is imperative that imperfect calibration and sidelobes associated with station beam-forming (used by LOFAR and MWA) not introduce spectral structure that impedes foreground removal. The trade-off of per-station collecting area versus primary-beam smoothness is one of the major design parameters that must be addressed by first-generation experiments to lead into a next-generation instrument such as phase-II of the Hydrogen Epoch of Reionization Array⁵ (HERA; Comm. for a Decadal Survey of A&A; NRC 2010) and the Square Kilometer Array⁶ (SKA). In all cases, first-generation experiments will be starved for sensitivity, motivating the exploration of techniques for improving sensitivity.

Optimizing these design parameters for future 21cm EoR arrays requires a careful assessment of the trade-offs between sensitivity and facility of calibration in first-generation experiments. To further this investigation, we provide in §2 a detailed pedagogical derivation of the sensitivity for an interferometer targeting the 21cm reionization signal. Within this section, we relate sensitivity to the number of repeated measurements of modes in the uv -plane, motivating sampling redundancy as an important metric of the sensitivity performance of an array. In §3, we explore the conflicting goals of arrays aiming to characterize foregrounds and those aiming to measure the evolving power spectrum of reionization fluctuations. We then show how antenna placement can be used to tune sensitivity relative to bright foregrounds. We evaluate several antenna configurations to arrive at a class of configurations that maximize sensitivity to the 21cm EoR signal. Finally, in §4, we discuss how our configuration studies, along with experience with the technical challenges of foreground removal and correlating many antennas, will influence the design of future experiments targeting the 21cm EoR signal.

2. Sensitivity to the 21cm Power Spectrum

Although derivations of the sensitivity of a radio interferometer to the expected 21cm EoR signal exist in the literature (Morales 2005; McQuinn et al. 2006; Pen et al. 2009), we aim to clarify the derivation and be more precise about the approximations that have been made implicitly in previous derivations. The goals of this section are to develop a framework for comparing sensitivity to foregrounds that are often related in Jy units, to highlight the effects of wide fields-of-view and wide bandwidths on the approximations that are made, and to be as clear as possible about Fourier transform normalizations while deriving the sensitivity of an interferometric baseline to the

⁵<http://reionization.org/>

⁶<http://www.skatelescope.org/>

three-dimensional power spectrum of 21cm reionization.

2.1. Single-Baseline Response

We begin with the basic definitions for the 3D power spectrum of brightness temperature fluctuations (the statistic which 21cm efforts aim to measure) and for the visibility (the fundamental observable of an interferometer). We then calculate the response of a single interferometric baseline to the 21cm brightness-temperature fluctuations arising from cosmic reionization, thereby deriving the relationship between visibilities calibrated to a Jy scale and reionization fluctuations in k -space expressed in mK^2 units. For this derivation, we adopt a Fourier transform normalization convention that is consistent with that used in theoretical models (and is standard in cosmological work), but which differs from that used in radio astronomy. With respect to the brightness temperature in a pixel of the sky plane/frequency data cube, $T(\vec{x})$, and its Fourier dual $\tilde{T}(\vec{k})$, this convention yields:

$$\begin{aligned}\tilde{T}(\vec{k}) &= \frac{1}{\mathbb{V}} \int T(\vec{x}) e^{-i\vec{k}\cdot\vec{x}} d^3x \\ T(\vec{x}) &= \frac{\mathbb{V}}{(2\pi)^3} \int \tilde{T}(\vec{k}) e^{i\vec{k}\cdot\vec{x}} d^3k,\end{aligned}\tag{1}$$

Here, \mathbb{V} refers to the volume of the observed data cube and \vec{x} is a 3D vector that indicates direction on the sky and depth (the frequency dimension) within the field. Likewise, \vec{k} is a 3D wave-vector with projection $\vec{k}_\perp \equiv (k_x, k_y)$ in the plane of the sky, and k_z along the line-of-sight (frequency) direction. We derive our response in the flat-sky approximation (as discussed below) so that we may take \vec{x} to be cartesian.

It follows from this convention that an estimate of the power spectrum is given by

$$\hat{P}(\vec{k}) \equiv \langle |\tilde{T}(\vec{k})|^2 \rangle = \int \hat{\xi}(\vec{r}) e^{-i\vec{k}\cdot\vec{r}} d^3r,\tag{2}$$

where angle brackets denote an ensemble average, \vec{r} is the vector distance between two points, and $\hat{\xi}(\vec{r})$ is an estimate of the two-point correlation function of the measured T , given by

$$\hat{\xi}(\vec{r}) = \frac{1}{\mathbb{V}} \int T(\vec{x}) T(\vec{x} + \vec{r}) d^3x.\tag{3}$$

It is important to note that the Fourier transform normalization defined by equation 2 is *not* consistent with the transformation defining the visibility for a single baseline (Morales & Hewitt 2004); a volume factor, \mathbb{V} , divides the integral in equation 2, but no observing volume appears in the denominator of the following definition of the visibility adapted from Thompson (1999), their equation (2-21):

$$\begin{aligned}V(u, v, w, \nu) &\equiv \int \frac{dl dm}{\sqrt{1-l^2-m^2}} A(l, m, \nu) I(l, m, \nu) \\ &\times e^{-2\pi i(ul+vm+w[\sqrt{1-l^2-m^2}-1])},\end{aligned}\tag{4}$$

where ν is spectral frequency, $l \equiv \sin \theta_x$ and $m \equiv \sin \theta_y$ are (in the small-angle approximation) angular coordinates in image domain, $(u, v, w) \equiv \vec{b}/\lambda$ are the east-west, north-south, and line-of-sight projections of baseline vector \vec{b} toward a phase center, in units of observing wavelength λ , $A(l, m, \nu)$ is a windowing function describing the field-of-view and bandpass response of an interferometer pair, and $I(l, m, \nu)$ is the specific intensity.

It is common to neglect the (l, m) -dependence of the w -term in the exponential — a simplification commonly referred to as the flat-sky approximation (Clark 1999). This approximation is valid within a radius $\approx 10^\circ$ of the phase center or when phasing to a direction orthogonal to the baseline vector (so that $w \approx 0$). For many low-frequency arrays, including PAPER, wide fields-of-view make this approximation invalid, and proper imaging requires techniques such as W-projection (Cornwell et al. 2003). However, the magnitude of the 21cm EoR power spectrum $P_{21}(\vec{k})$ is not expected to evolve significantly over $k \pm |k_\perp|$ for baselines shorter than 300 meters. Hence, the linear combination of \vec{k} -modes generated by the point-spread function (PSF) of a baseline⁷ is still representative of the statistical distribution described by $P_{21}(k)$. We adopt the flat-sky approximation for simplicity, but use the full area of the primary beam to estimate sensitivity.

To relate Fourier transform conventions that differ by a factor of integration volume, we extend the definition of the visibility in the flat-sky approximation to include a similar Fourier transform along the frequency axis:

$$\begin{aligned} \tilde{V}(u, v, \eta) \approx & \int dl dm d\nu A(l, m, \nu) I(l, m, \nu) \\ & \times e^{-2\pi i(u l + v m + \eta \nu)}. \end{aligned} \quad (5)$$

This definition ignores the frequency-dependence of (u, v) arising from the changing length of λ dividing the physical separation of two antennas. 21cm EoR experiments have large relative bandwidths, with (u, v) varying by as much as 4% over a 6-MHz bandwidth at 150 MHz. The 4% variation in the \vec{k}_\perp component of \vec{k} that arises from the frequency-dependence of (u, v) is smaller than the averaging interval used later in §2.3, and approximation does not substantially affect sampling of $P_{21}(\vec{k})$, nor does it change the sensitivities we derive. Of greater concern in our examination of the frequency-dependent sampling of the uv -plane by a single baseline is the effect it may have on foreground removal. We will revisit this issue briefly in §3, but we defer a detailed

⁷ From the perspective of deriving the power-spectrum response of a single baseline, the dominant effect of violating the flat-sky approximation is that the fringe-pattern of the baseline (which is a sinusoid in l, m) gradually de-tunes from a cartesian sinusoid away from phase center. As a result, a Fourier mode at (u, v) that is sampled by a baseline will have a PSF in \vec{k} -space that is peaked in \vec{k}_\perp , but which includes contributions from modes with smaller $|\vec{k}_\perp|$ that project onto the fringe pattern nearer to the horizon. The degree of peaked-ness depends on the relative gain of the primary beam within the region where the flat-sky approximation is valid. For nearly all of the \vec{k} -modes accessible to 21cm EoR instruments, $|\vec{k}|$ is dominated by the line-of-sight component k_z . It follows from equations 17 and 18 that for line-of-sight scales arising from a 6-MHz bandwidth, the \vec{k}_\perp component arising from a 300-m baseline perturbs $|\vec{k}|$ by $\Delta \ln k \leq 0.5$, falling within the fiducial averaging interval used in §2.3. This perturbation decreases rapidly for shorter baseline lengths.

treatment of the subject to a future paper.

Squaring both sides and using $I = 2k_B T / \lambda^2$, with λ being the mean wavelength over the sub-band used in the Fourier transform, yields

$$\begin{aligned} \tilde{V}^2(u, v, \eta) &\approx \left(\frac{2k_B}{\lambda^2}\right)^2 \int dl dm d\nu dl' dm' d\nu' \\ &\times A(l, m, \nu) T(l, m, \nu) A(l', m', \nu') T(l', m', \nu') \\ &\times e^{-2\pi i[u(l-l') + v(m-m') + \eta(\nu-\nu')]}. \end{aligned} \quad (6)$$

We now make the approximation that $A(l, m, \nu)$ is a top-hat windowing function. Explicitly integrating $A(l, m, \nu)$ determines the width and shape of the convolution kernel in equation 11. Since the width of this kernel is thereafter neglected and only enters later to tally the number of independent wave-modes sampled, the top-hat approximation should be considered purely pedagogical. Drawing $A(l, m, \nu)$ into the bounds of the integral yields:

$$\begin{aligned} \tilde{V}^2(u, v, \eta) &\approx \left(\frac{2k_B}{\lambda^2}\right)^2 \int_{(0,0,0)}^{(\theta,\theta,B)} dl dm d\nu \int_{(0,0,0)}^{(\theta,\theta,B)} dl' dm' d\nu' \\ &\times T(l, m, \nu) T(l', m', \nu') e^{-2\pi i[u(l-l') + v(m-m') + \eta(\nu-\nu)]}, \end{aligned} \quad (7)$$

where $\theta \equiv \sqrt{\Omega}$, for primary beam field-of-view Ω . Changing variables so that $(l_r, m_r, \nu_r) = (l - l', m - m', \nu - \nu')$:

$$\begin{aligned} \tilde{V}^2(u, v, \eta) &\approx \left(\frac{2k_B}{\lambda^2}\right)^2 \left[\int_{(-\theta, -\theta, -B)}^{(0,0,0)} dl_r dm_r d\nu_r \int_{(0,0,0)}^{(\theta+l_r, \theta+m_r, B+\nu_r)} dl dm d\nu \right. \\ &\quad \left. + \int_{(0,0,0)}^{(\theta,\theta,B)} dl_r dm_r d\nu_r \int_{(l_r, m_r, \nu_r)}^{(\theta,\theta,B)} dl dm d\nu \right] \\ &\times T(l, m, \nu) T(l-l_r, m-m_r, \nu-\nu_r) e^{-2\pi i(ul_r + vm_r + \eta\nu_r)}. \end{aligned} \quad (8)$$

Integrating over (l, m, ν) and using equation 3 yields:

$$\begin{aligned} \tilde{V}_{21}^2(u, v, \eta) &\approx \left(\frac{2k_B}{\lambda^2}\right)^2 \Omega B \int_{(-\theta, -\theta, -B)}^{(\theta,\theta,B)} dl_r dm_r d\nu_r \\ &\times \hat{\xi}_{21}(l_r, m_r, \nu_r) e^{-2\pi i(ul_r + vm_r + \eta\nu_r)}, \end{aligned} \quad (9)$$

where B is the observing bandwidth, and where we now use the subscript “21” to make explicit that these quantities are derived for 21cm emission from reionization. Using X and Y to represent conversion factors from angle and frequency to comoving distance, respectively, we substitute $(Xl_r, Xm_r, Y\nu_r)$ for (r_x, r_y, r_z) and (Xk_x, Xk_y, Yk_z) for $2\pi(u, v, \eta)$. The factor of 2π follows from the cosmological Fourier convention. This substitution then yields

$$\tilde{V}_{21}^2(u, v, \eta) \approx \left(\frac{2k_B}{\lambda^2}\right)^2 \frac{\Omega B}{X^2 Y} \int_{(-X\theta, -X\theta, -YB)}^{(X\theta, X\theta, YB)} \hat{\xi}_{21}(\vec{r}) e^{-i\vec{k}\cdot\vec{r}} d^3r, \quad (10)$$

This equation establishes the relationship between a (u, v, η) -mode measured by an interferometer and a \vec{k} -mode. Hereafter we will use “ (u, v, η) -mode” and “ \vec{k} -mode” interchangeably to refer to a coherent region in Fourier space. Because the right-hand side of equation 10 is the Fourier transform of $\xi(\vec{r})$ with a top-hat window, in Fourier space it becomes the convolution of the Fourier transform of these functions:

$$\begin{aligned} \tilde{V}_{21}^2(u, v, \eta) \approx & \left(\frac{2k_B}{\lambda^2}\right)^2 \frac{\Omega B}{X^2 Y} \left[\hat{P}_{21}(\vec{k}) * (\text{sinc}(2X\theta k_x) \right. \\ & \left. \times \text{sinc}(2X\theta k_y) \text{sinc}(2YBk_z)) \right], \end{aligned} \quad (11)$$

where ‘ $*$ ’ signifies convolution in \vec{k} . In the more general case this convolving kernel is not a sinc function, but the Fourier transform of the primary beam $\tilde{A}(l, m, \nu)$. For primary beam responses larger than 30 arcmin, the width of the kernel in k -space is much smaller than the scales over which $P_{21}(\vec{k})$ varies for the k -modes that are likely not to be dominated by foregrounds (McQuinn et al. 2006). Thus, we drop the sinc kernel from equation 11, giving:

$$\tilde{V}_{21}^2(u, v, \eta) \approx \left(\frac{2k_B}{\lambda^2}\right)^2 \frac{\Omega B}{X^2 Y} \hat{P}_{21}(\vec{k}). \quad (12)$$

Theoretical studies often express the 21cm signal in a dimensionless manner given by $\hat{\Delta}^2(k) \equiv \frac{k^3}{2\pi^2} \hat{P}(\vec{k})$ (using that $P_{21}(\vec{k})$ is expected to be nearly isotropic; McQuinn et al. 2006), making it useful to write equation 12 as

$$\tilde{V}_{21}^2(u, v, \eta) \approx \left(\frac{2k_B}{\lambda^2}\right)^2 \frac{\Omega B}{X^2 Y} \frac{2\pi^2}{k^3} \hat{\Delta}_{21}^2(k). \quad (13)$$

2.2. Single-Baseline Sensitivity Measuring One \vec{k} -mode

The next step towards estimating the sensitivity to the 21cm signal is to calculate the power spectrum of the thermal noise of an instrument. Thermal fluctuations produce a white-noise signal with root-mean-square (RMS) brightness temperature $T_{N,\text{rms}}$, which in practice will be roughly equal to the sky temperature for 21cm instruments. The thermal noise contributes a component to the RMS amplitude of the visibility \tilde{V}_N equal to:

$$\tilde{V}_N = \frac{2k_B}{\lambda^2} T_{N,\text{rms}} \Omega B. \quad (14)$$

This equation can be derived from equation 4 assuming a white-spectrum thermal noise for I with temperature $T_{N,\text{rms}}$. We substitute \tilde{V}_N for \tilde{V} in equation 13 to get the noise contribution⁸ to the

⁸ When squaring \tilde{V} in equation 13, it is important to construct an estimator of $\Delta_{21}^2(k)$ that is not biased by the noise power spectrum. This can be accomplished by subtracting off a measured noise power spectrum, or more elegantly by constructing cross-products $\tilde{V}_i \tilde{V}_j^*$ from pairs of samples i, j that measure the same Fourier mode but have independent thermal noise. The sensitivities that are derived here reflect the residual error that remains in an *unbiased* construction of \tilde{V}^2 .

dimensionless power, $\Delta_{\text{N}}^2(k)$, yielding:

$$\Delta_{\text{N}}^2(k) \approx X^2 Y \frac{k^3}{2\pi^2} \Omega B T_{\text{N,rms}}^2(u, v, \eta). \quad (15)$$

Since there are $2Bt$ independent measurements of the noise for time t , the value of $T_{\text{N,rms}}$ noise that should enter in equation 15 is not the true temperature at any given time (which is usually called the system temperature T_{sys}), but rather the error in how well T_{sys} can be measured (which relates to the error in how well thermal noise can be measured and subtracted off, and is $\sqrt{2}T_{\text{sys}}$ for Gaussian random noise) or $T_{\text{N,rms}}^2 = T_{\text{sys}}^2/Bt$. With this substitution,

$$\Delta_{\text{N}}^2(k) \approx X^2 Y \frac{k^3}{2\pi^2} \frac{\Omega}{2t} T_{\text{sys}}^2, \quad (16)$$

where t is the integration time for sampling a particular (u, v, η) -mode, and the factor of two in the denominator comes from the explicit inclusion of two orthogonal polarizations to measure the total unpolarized signal.⁹ This equation differs from the derivations given in Morales (2005) and McQuinn et al. (2006) by only this polarization factor. Note how the power-spectrum sensitivity toward a particular \vec{k} -mode is independent of bandwidth, and that (Furlanetto et al. 2006)

$$X \approx 1.9 \left(\frac{1+z}{10} \right)^{0.2} h^{-1} \frac{\text{Mpc}}{\text{arcmin}} \quad (17)$$

$$Y \approx 17 \left(\frac{1+z}{10} \right)^{\frac{1}{2}} \left(\frac{\Omega_m h^2}{0.15} \right)^{-\frac{1}{2}} \frac{\text{Mpc}}{\text{MHz}}, \quad (18)$$

giving us (for $\Omega_m = 0.27$):

$$X^2 Y \approx 540 \left(\frac{1+z}{10} \right)^{0.9} h^{-3} \frac{\text{Mpc}^3}{\text{sr} \cdot \text{Hz}}. \quad (19)$$

Substituting for $X^2 Y$ at $z = 8.5$ (assuming observations at 150 MHz) in equation 16, and choosing fiducial PAPER parameters, we have:

$$\begin{aligned} \Delta_{\text{N}}^2(k) \approx & 2.8 \times 10^4 \left[\frac{k}{0.1h \text{ Mpc}^{-1}} \right]^3 \left[\frac{\Omega}{0.76 \text{ sr}} \right]^{\frac{3}{2}} \\ & \times \left[\frac{T_{\text{sys}}}{500 \text{ K}} \right]^2 \left[\frac{120 \text{ days}}{t_{\text{days}}} \right] \left[\frac{|\vec{u}|}{20} \right] \text{ mK}^2, \end{aligned} \quad (20)$$

where we assume 120 days of observation with a baseline of length $|\vec{u}| \sim 20$ that allows ~ 13 minutes of integration per day, for a total integration time of 9×10^4 seconds per (u, v, η) -mode.

⁹ As defined above, $\Delta_{\text{N}}^2(k)$ indicates the noise left in the map after one tries to subtract the noise power using all of the available information. It may be defined equivalently as relating to the signal-to-noise at which the true power spectrum, $\Delta_{21}^2(k)$, can be measured in a k -bin: $\text{SNR} = \Delta_{21}^2(k)/\Delta_{\text{N}}^2(k)$. This definition assumes that Δ_{N}^2 is calculated for a real-valued sky, so that baselines sampling positive and negative Fourier components are not counted as independent measurements.

In general, integration time per mode, per day depends strongly on baseline orientation and the latitude at which an array is deployed. We will estimate a minimum integration timescale here for arrays at mid-latitudes, and defer an exact, configuration-dependent treatment until §2.4 and §3. We compute the amount of time a baseline samples a (u, v, η) -mode per day, $t_{\text{per_mode}}$, as it is limited by the timescale for earth-rotation to move the sampling of a baseline a distance of $\Omega^{-1/2}$ in the uv -plane: $t_{\text{per_mode}} \approx 1/\sqrt{\Omega\omega_{\oplus}}|\vec{u}|$, where ω_{\oplus} is the angular speed of the earth’s rotation. The choice of 20 wavelengths as a fiducial baseline length is arbitrary, but represents an estimate of a minimum baseline length that is not dominated by galactic synchrotron emission (see §3.2).

The cosmological 21cm signal is typically much smaller than the noise in a single baseline, as given by equation 20. This assumption is reflected in our derivation by the absence of sample variance as a significant contribution to the errors we compute. The globally averaged spin temperature of the 21cm transition is $\langle T_{21} \rangle = 28 ([1 + z]/10)^{1/2}$ mK for neutral intergalactic medium, assuming that the spin temperature of the 21cm transition is much larger than the cosmic microwave background (CMB) temperature (which will almost certainly hold at $z < 10$; e.g. Furlanetto et al. 2006). For a patchy reionization process, an estimate for the dimensionless power spectrum of 21cm fluctuations arising from inhomogeneities in the ionization fraction is given by

$$\Delta_{21cm}^2 \sim \langle T_{21} \rangle^2 (x_H - x_H^2) / \ln(k_{\text{max}}/k_{\text{min}}), \quad (21)$$

where x_H is the average neutral hydrogen fraction and k_{min} and k_{max} are the wave-vectors between which most of the power lies. Consistent with this estimate, when $x_H \approx 0.5$, simulations of reionization find $10 < \Delta_{21}^2 < 100$ mK² with a flat spectrum over $0.1 < k < 10$ h Mpc⁻¹ (McQuinn et al. 2007; Trac & Cen 2007). Models with rarer sources tend to produce larger ionized regions and more power than those with more abundant sources (McQuinn et al. 2007). Comparing equation 21 to the sensitivity of a baseline in equation 20 motivates the exploration of methods for bolstering the sensitivity of instruments to the 21cm EoR signal.

Before proceeding, it is worth reiterating the assumptions that went into the previous derivation, and to consider any generality that may have been lost:

1. We assumed we could work in the flat sky limit, which we justified by noting that the 21cm EoR power spectrum $P_{21}(k)$ is not expected to evolve on the scale of the mode-mixing introduced by this approximation.
2. We ignored the frequency dependence of the (u, v) -coordinates of a baseline for the same reason. For baselines longer than ≈ 300 m, both of the above assumptions break down and cause errors at the several percent level.
3. We pedagogically treated the antenna primary beam as top-hat function, but argued that any primary beam with FWHM wider than 30 arcmin creates a sufficiently small convolving kernel in equation 11 that its shape may be neglected.

4. We have assumed the SNR in any individual \vec{k} -mode measurement to be much less than unity. Since any additional improvement to sensitivity comes from independent \vec{k} -modes whose inclusion beats down both thermal fluctuations and sample variance, this assumption in effect allows us to ignore sample variance as a significant source of error.
5. Finally, our value of observing time per mode in equation 20 represents a lower bound; its exact value generally depends on baseline orientation and array latitude and must be computed explicitly for specific EoR experiment locations and configurations.

2.3. Combining Independent \vec{k} -mode Measurements

With the sensitivity of one baseline to one \vec{k} -mode derived, we now turn our attention to the sensitivity boost that comes from combining multiple baselines. In this section, we consider an analytically tractable case, where each baseline measures an independent \vec{k} -mode. Statistically independent \vec{k} -modes can be combined to improve sensitivity proportionally to the square root of the number of samples, $N_s^{1/2}$. We ignore sampling redundancy — the possibility that many baselines can measure the same \vec{k} -mode — which closely approximates the response of minimum-redundancy arrays used for imaging (see §3.1). Although somewhat contrived, this example demonstrates how several different sensitivity boosts that arise from system and observing parameters. In §2.4 we will use numerical simulations to calculate the sensitivities of real array configurations, including sampling redundancy.

Several assumptions are used to make this derivation tractable. The final expression derived in this section — equation 25 — is not intended to be generally applicable, but rather to illustrate the different effects that come into play when combining measurements. The fully general case is presented in equation 27, where one must numerically calculate the effects of array configuration. Our principal assumption is that our baselines uniformly sample the uv -plane within a radius u_{\max} . As before, we also assume that our baselines are short enough to neglect to contribution of k_{\perp} to \vec{k} , generally true for baselines under 300m. Finally, using PAPER as a model, we assume an array at $45^{\circ}N/S$ latitude observing for six sidereal hours per day ($t_{\text{per.day}}$ below) during which colder patches of the synchrotron sky are overhead. Since we assume no sampling redundancy, it is irrelevant whether these six hours of observation are spent tracking a single phase center or are broken up into several observations with different pointings.

Before we discuss the different sources of independent \vec{k} -mode samples, we define a fiducial measurement which all improvements are relative to. In this section, we use equation 20, the sensitivity of one baseline measuring one \vec{k} -mode as our benchmark. We will refer to the new noise level after combining measurements as $\Delta_{\text{N}}^2(k)$ and express this value relative to our fiducial value, $\Delta_{\text{N},0}^2(k)$.

We now will outline the different sources of independent \vec{k} -mode samples and present physical arguments for their dependencies on various parameters. A full derivation, including the prefactor

of the final sensitivity result in equation 25, is presented in Appendix A.

1. **Multiple line-of-sight samples** One source of independent \vec{k} -mode samples comes from the many line-of-sight Fourier modes measured by a single baseline; since $\Delta_{21}^2(k)$ is expected to evolve on $\log-k$ scales, data may be binned in equally-spaced $\Delta \ln k$ intervals, so that $N_s(k) \propto k$. For example, with 6-MHz observing bandwidth, B , a single baseline will sample $k \approx 0.06h \text{ Mpc}^{-1}$ once, $k \approx 0.12h \text{ Mpc}^{-1}$ twice, etc. This linearly increasing number of independent samples versus k produces a $\text{SNR} \propto k^{1/2}$ scaling. The number of samples within a bin is also dependent on the bin size, giving rise to a final proportionality after combining line-of-sight modes:

$$\Delta_{\text{N}}^2(k) \propto \left[\frac{1}{k} \right]^{\frac{1}{2}} \left[\frac{1}{B} \right]^{\frac{1}{2}} \left[\frac{1}{\Delta \ln k} \right]^{\frac{1}{2}} \Delta_{\text{N},0}^2(k) \quad (22)$$

2. **Multiple time samples** Another source of independent measurements comes from the number of time bins available for measuring $\Delta_{21}^2(k)$ in a sidereal day. These additional samples grow linearly with the daily observation length, $t_{\text{per.day}}$. (Accumulating samples over multiple days was already accounted for in equation 20.) Therefore, the sensitivity increases as:

$$\Delta_{\text{N}}^2(k) \propto \left[\frac{1}{t_{\text{per.day}}} \right]^{\frac{1}{2}} \Delta_{\text{N},0}^2(k) \quad (23)$$

3. **Multiple uv-plane samples** A final source of independent samples comes from baselines sampling different regions of the uv -plane. The most straightforward way these samples affect the sensitivity is through adding more baselines. Each baseline is an independent measurement, so sensitivity grows as the square root of number of baselines, or, linearly with the number of antennas, N .

Secondly, we need to add up all the measurements across the uv -plane. Using our assumption that uv -samples are uniformly distributed within a circle of radius u_{max} in the uv -plane, we integrate contributions from rings of constant $|\vec{u}|$ up to a distance $|\vec{u}| = u_{\text{max}}$. This integration is simplified by noting that each ring of constant $|\vec{u}|$ contributes equally to the sensitivity of the final measurement; as $|\vec{u}|$ increases, the reduction in coherent integration time per (u, v, η) -mode is offset by the increasing number of baselines sampling within that ring. Integrating a constant sensitivity contribution versus $|\vec{u}|$ gives rise to a $u_{\text{max}}^{1/2}$ term in the resulting residual noise estimate for minimum-redundancy arrays.

There is also a factor of solid beam angle $\Omega^{-1/4}$, which is a combination of two factors. First, there is a decrease in integration time per (u, v, η) -mode associated with a broader primary beam, which scales as the width of the primary beam, $\Omega^{-1/2}$. This term is somewhat offset by a second factor: the increased number of independent modes sampled, contributing a factor of $\Omega^{1/4}$ to sensitivity. The result is:

$$\Delta_{\text{N}}^2(k) \propto u_{\text{max}}^{\frac{1}{2}} \left[\frac{1}{\Omega} \right]^{\frac{1}{4}} \left[\frac{1}{N} \right]^{\frac{1}{2}} \Delta_{\text{N},0}^2(k) \quad (24)$$

Combining all these different gains from binning the data with the prefactor calculated in Appendix A yields the final result of this section:

$$\begin{aligned} \Delta_{\text{N}}^2(k) &\approx 150 \left[\frac{k}{0.1h \text{ Mpc}^{-1}} \right]^{\frac{5}{2}} \left[\frac{6 \text{ MHz}}{B} \right]^{\frac{1}{2}} \left[\frac{1}{\Delta \ln k} \right]^{\frac{1}{2}} \\ &\times \left[\frac{\Omega}{0.76 \text{ sr}} \right]^{\frac{5}{4}} \left[\frac{T_{\text{sys}}}{500 \text{ K}} \right]^2 \left[\frac{6 \text{ hrs}}{t_{\text{per.day}}} \right]^{\frac{1}{2}} \\ &\times \left[\frac{120 \text{ days}}{t_{\text{days}}} \right] \left[\frac{u_{\text{max}}}{20} \right]^{\frac{1}{2}} \left[\frac{32}{N} \right] \text{ mK}^2, \end{aligned} \quad (25)$$

2.4. The Sensitivity Benefits of Redundant uv -Sampling

As mentioned above, sensitivity to $\Delta_{21}^2(k)$ depends on both the sensitivity obtained in individual (u, v, η) -mode bins and the number of bins sampled. As discussed in the context of CMB analysis, sensitivity is most efficiently improved by integrating coherently on select modes until $\text{SNR} \sim 1$ is obtained, whereupon sampling additional modes to beat down sample variance in the cosmological signal becomes the most efficient way of improving sensitivity (Park et al. 2003). Equation 20 suggests that the PAPER experiment, along with many other first-generation 21cm EoR experiments (McQuinn et al. 2006), will be firmly in the $\text{SNR} < 1$ regime for individual modes for the near future. As a result, it is natural to explore how sensitivity might be improved by choosing antenna configurations that maximize the degree to which uv -bins are sampled by multiple baselines.

In this section, we outline a formalism for computing the sensitivity boost of a generic antenna array, expressed in terms of a redundancy metric that tracks sensitivity relative to a fiducial measurement, which we choose to be a single baseline with a one-second integration. The choice of fiducial integration time is arbitrary, but affects the scaling constants in the equations that follow.

Next, we define a metric for the sampling redundancy generated by an array,

$$\frac{f}{f_0} \equiv \frac{\sum_i n_i^2}{\sum_i n_i}. \quad (26)$$

where f_0 is the sampling redundancy of a single baseline with a one-second integration and n_i represents the number of one-second samples falling in uv -bin i . The ratio f/f_0 measures the increase in sensitivity for a redundant array over one in which there is no sampling redundancy. We motivate the definition of sampling redundancy in Appendix B and show that sensitivity increases as $\sqrt{f/f_0}$.

The instantaneous (single-integration) redundancy of an array ranges from f_0 to Nf_0 , where N is the number of antennas in an array configured for the densest non-overlapping packing of antennas possible in two dimensions: a filled circular aperture; we derive this case in Appendix B.3. However, computing the instantaneous redundancy of an array does not account for any additional

redundancy that may be generated through earth-rotation synthesis. A baseline sampling a non-redundant uv -bin can, some time later, migrate in the uv -plane to sample a bin already sampled by another baseline. Generally, the redundancy generated through earth-rotation synthesis depends strongly on antenna configuration. We will rely on numerically computed redundancies for specific configurations.

We include the effect of sampling redundancy by using f defined for one-second integrations toward a transiting phase center, calculated from equation 16. Our result in equation 27 (which is derived in full in Appendix B), is expressed in terms of fiducial observation and array parameters. Unlike equation 25, the effects of array configuration are now captured in the computed value for f :

$$\begin{aligned} \Delta_N^2(k) \approx & 60 \left[\frac{k}{0.1h \text{ Mpc}^{-1}} \right]^{\frac{5}{2}} \left[\frac{6 \text{ MHz}}{B} \right]^{\frac{1}{2}} \left[\frac{1}{\Delta \ln k} \right]^{\frac{1}{2}} \\ & \times \left[\frac{\Omega}{0.76 \text{ str}} \right] \left[\frac{T_{\text{sys}}}{500 \text{ K}} \right]^2 \left[\frac{6 \text{ hrs}}{t_{\text{per.day}}} \right]^{\frac{1}{2}} \\ & \times \left[\frac{120 \text{ days}}{t} \right] \left[\frac{32}{N} \right] \left[\frac{10^4 f_0}{f} \right]^{\frac{1}{2}} \text{ mK}^2, \end{aligned} \tag{27}$$

The value of f/f_0 varies substantially with N and for different antenna configurations. An array without redundant sampling will have $f/f_0 = 1$. A nominal value of $f/f_0 = 3.4 \times 10^4$, representative of the antenna configurations considered later, yields $\Delta_N^2(k) \approx 33 \text{ mK}^2$ at $k = 0.1h \text{ Mpc}^{-1}$. As described in §2.3, we assume six-hour observations. For PAPER, these observations are phased to transit pointings separated by two hours and are accumulated into separate (u, v, η) -bins for each pointing. (Two hours corresponds to the approximate width of the PAPER primary beam, after which a new, statistically independent region of sky dominates the data). Since there can be no redundancy between samples from different pointings, this has the effect of somewhat reducing f . Generally, f accounts for most effects relating to observing strategy.

3. Antenna Configuration Studies

Designers of interferometric arrays for sonar, radar, and radio astronomy applications have long appreciated the necessity of carefully choosing the physical placement of array elements to produce desirable samplings of the uv -plane. One of the most popular criteria — the minimization of image-domain sidelobes arising from incomplete sampling — motivates array designs that maximize the number of independent Fourier modes sampled, or equivalently, minimize the redundancy with which uv -pixels are sampled. Such *minimum-redundancy* configurations are valuable for characterizing point-source foregrounds to the 21cm EoR signal, since each uv -pixel provides unique information for constraining the image-domain distribution of flux density. All sampled Fourier modes contribute to each image-domain location, making sensitivity independent of antenna arrangement within a fixed maximum baseline length for image-domain measurements. This

gives rise to the traditional adaptation of the radiometer equation for interferometers (see Wrobel & Walker 1999, their equation 9-23):

$$T_{\text{rms}}\Omega_s = \frac{T_{\text{sys}}\Omega}{\sqrt{BtN(N-1)}} \quad (28)$$

where Ω_s , the angular size of a synthesized beam, is implicitly related to maximum baseline length.

In contrast, the sensitivity of Fourier-domain measurements *do* depend dramatically on array configuration. First-generation experiments will constrain the power-spectrum of 21cm EoR fluctuations by sampling \vec{k} -modes accessed via spectral structure in sampled uv -pixels. As discussed in §2.4, sensitivity-limited arrays will do best by redundantly sampling a select number of uv -pixels. However, *maximum-redundancy* array configurations run directly counter to the needs of image-domain work, and will look counter-intuitive to those familiar with standard minimum-redundancy array configurations.

In §2.1, we discussed how a single baseline measures $\Delta_{21}^2(k)$ at a range of k -scales with the approximation that (u, v) are not frequency dependent, and argue that this approximation does not dramatically affect response to the 21cm EoR signal. The impact of frequency-dependent sampling on foreground response is somewhat more concerning, and has been used to argue for configurations that produce uniform sampling of the uv -plane (Bowman et al. 2009). Such sampling could permit chosen uv -modes to be sampled continuously versus frequency, even if the baseline sampling them changes. In a future paper, we will explore in detail the effects of frequency-dependent uv -sampling, showing that for baselines shorter than ~ 100 wavelengths, all but the smallest k -modes are accessible using the inherent frequency-dependent uv -sampling produced by a baseline. This forthcoming result contrasts with the view that 21cm EoR arrays must produce uniform uv -coverage and motivates the exploration of other maximum-redundancy array configurations. With an eye toward using the inherent frequency-dependent sampling of each baseline independently to sample $\Delta_{21}^2(k)$, we largely ignore the frequency dependence of array sampling in the discussion of maximum-redundancy arrays; redundant sampling will be redundant at all frequencies.

Both minimum- and maximum-redundancy configurations have valuable properties for 21cm EoR work. Array configurations aiming to incorporate aspects of both must attempt to strike a balance between their opposing influences. Where this balance lies depends on the relative immediacy of sensitivity and foreground-removal needs. Given our current ignorance of many foreground properties, it is most straightforward to consider each type of configuration separately, as we will below.

3.1. Minimum-Redundancy Array Configurations

Designing a minimum-redundancy antenna configuration reduces to choosing a real-valued sampling function $\mathcal{A}(x, y)$, with Fourier dual $\tilde{\mathcal{A}}(u, v)$, such that $\int |\tilde{\mathcal{A}}|^2 du dv$ is minimized. This optimization problem is usually discretized by sampling the aperture plane on the scale of the

aperture of a single antenna element, and by assuming $\mathcal{A}(x, y)$ to be unity-valued at a location containing an antenna element and zero-valued elsewhere. We are often interested in dense packings of antennas that also minimize the maximum distance of uv -samples from the origin. Compact packings of antennas have the desirable property of sampling nearly all Fourier modes for a targeted angular resolution. Compact minimum-redundancy configurations can also be trivially scaled to larger physical spacings to sample smaller angular scales.

A fact that may be under-appreciated in the radio astronomy community is that this optimization problem has many parallels with Golomb rulers (Sidon 1932; Babcock 1953), Golomb rectangles (Robinson 1985), and Costas arrays (Costas 1984) — mathematical constructions originally motivated by radar and sonar applications. Investigation of Golomb rulers and Costas arrays are active fields of mathematical research with interesting applications (Golomb & Gong 2004). In particular, the study of Costas arrays ($N \times N$ matrices with elements chosen such that no two elements share a row or column and such that the displacement vector between each pair of elements is unique) has yielded algorithms for generating minimum-redundancy arrays where N is near a prime number (Golomb & Taylor 1984). For generating array configurations, directly computing antenna locations following construction algorithms for Costas arrays is a vast improvement over the iterative optimization approaches presented in the literature (Keto 1997; de Villiers 2007).

Although Costas arrays do not quite capture the full minimum-redundancy optimization problem (they omit samplings along the u and v axes and they do not attempt to optimize how compactly antennas are placed), they do sample approximately one-quarter of the available uv -plane without redundancy. This filling fraction exceeds what has been demonstrated with other approaches in the literature. For comparison, we examine the dithered Reuleaux-triangle approach favored by Keto (1997) for generating configurations with uniform uv -coverage, scaled to the size of an equivalent Costas array (in this case, for $N = 24$) to remove scale-dependence in the redundancy metric. As we show in Figure 1, this configuration redundantly samples 28 locations with its instantaneous zenith-phased uv -coverage. For imaging point sources in the high-SNR limit, this configuration loses 6.7% of the information accessed by a roughly equivalent configuration derived from a Costas array.

As an example of a larger-sized minimum-redundancy configuration derived from a Costas array, we produce the $N = 36$ antenna configuration shown in the upper-left panel of Figure 1 following the Welch construction (Golomb & Taylor 1984), where N is chosen to be one less than the prime $p = 37$. According to this construction, we choose an integer $\alpha = 35$ with the property that $0 < \alpha \leq p$ such that $\alpha^N \bmod p = 1$ and $\alpha^i \bmod p \neq 1$ for $0 < i < N$. This construction produces row and column indices $(i, \alpha^i \bmod p)$ for placing antennas on an $N \times N$ grid. Note that $(i, \alpha^{i+j} \bmod p)$ also produces a Costas array for $0 \leq j < p$. Figure 1 illustrates the antenna configuration generated from a Costas array with $j = 23$, chosen so that the resulting configuration could be augmented with one more antenna (see the upper-left panel of Figure 1) without incurring any redundancy¹⁰.

¹⁰ For certain Costas arrays, relaxing the restriction that no two elements share a row or column allows one more

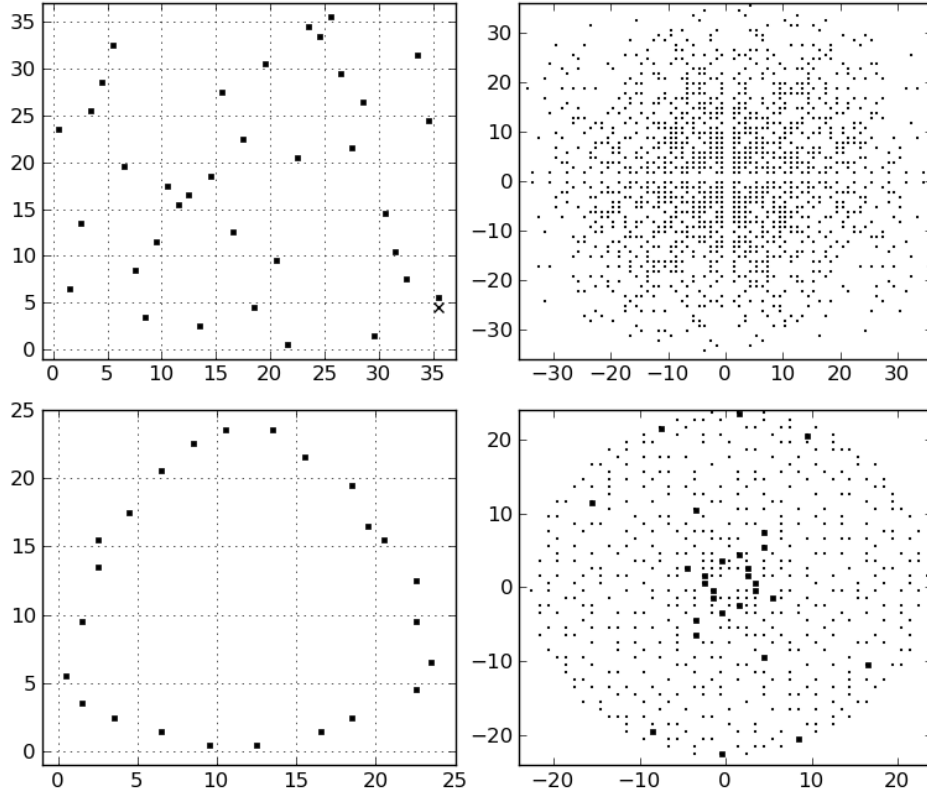


Fig. 1.— The top-left panel shows a minimum-redundancy antenna configuration based on an $N = 36$ Costas array (see §3.1). The associated instantaneous zenith-phased coverage of the uv -plane is shown in the top-right panel. For comparison, the bottom-left panel shows a 24-antenna configuration derived from a Reuleaux triangle that was iteratively optimized to generate uniform uv -coverage (Keto 1997). This configuration has been scaled for comparison to the size of a 24×24 Costas array to remove the effect of physical scale on the redundancy metric. The uv -coverage of this configuration (bottom-right panel) highlights the 28 redundant samplings with larger dots. Contrast this with Costas arrays, which are perfectly non-redundant and have simple construction algorithms for numbers of antennas near prime numbers. The “x” in the top-left panel shows where a 37th antenna can be introduced without generating redundant sampling if we relax the constraint that Costas arrays must have only one antenna per row and column. The antenna layout in the top-left panel, including the additional antenna, is scaled to grid spacings of 3.75 meters and 8 meters in the configurations labeled `min37c` and `min37`, respectively, in Figures 2, 3, 4, and 5.

For comparison with other antenna configurations, we generate two realizations of this minimum-redundancy configuration: one using 3.75-meter spacing between rows and columns (`min37c`), and one using 8-meter spacing that would be of more practical use for imaging foregrounds (`min37`). The performance of these configurations are compared with maximum-redundancy configurations in Figures 4 and 5. Costas arrays efficiently generate minimum-redundancy arrays for imaging, but these figures demonstrate that the minimal redundancy of these arrays has negative repercussions for power-spectrum sensitivity.

3.2. Maximum Redundancy Arrays

As shown in §2.4, sensitivity may be gained by focusing limited collecting area on specific modes of the power spectrum. However, the rising contribution of galactic synchrotron emission at large angular scales, the dominance of point-source emission at small angular scales, and the expectation that low-order line-of-sight (smooth-frequency) components must be used to suppress foregrounds suggest that array configuration must be informed by foreground characterization. Compact antenna configurations improve sensitivity by increasing sampling redundancy, motivating the centrally-condensed configurations explored for interferometers targeting the 21cm EoR signal (Bowman et al. 2006; Lidz et al. 2008). Such configurations, however, suffer from a number of practical deficiencies for this application:

1. The low fringe-rates associated with baselines sampling small $|\vec{u}|$ modes impede the discrimination of celestial signals from instrumental systematics (e.g. crosstalk).
2. Phase and gain self-calibration are compromised by the lack of longer baselines.
3. Proximity of antenna elements can cause cross-coupling, producing antenna-specific deviations in primary beam response.
4. Foreground emission peaks in brightness at the small $|\vec{u}|$ -modes that are most heavily sampled by centrally-condensed configurations.

Phase switching can help mitigate (though not eliminate) crosstalk, and incorporating a relatively small number of antennas at longer spacings can improve phase and gain calibration from point sources. Increasing the spacing between densely packed antennas can substantially decrease cross-coupling at the expense of the redundancy generated from earth-rotation synthesis. The fact that foreground emission peaks at small $|\vec{u}|$ is unavoidable.

antenna to be placed within the $N \times N$ matrix of possible locations, generating new uv -samples without incurring sampling redundancy. Such augmentations can be tested for in a Costas array by first computing the uv -sampling matrix for a Costas array (done by convolving the antenna placement pattern with itself) and then convolving the result with the original antenna placement pattern. A zero value within the original $N \times N$ matrix indicates a location where an antenna can be added without increasing sampling redundancy. Many Costas arrays may be created to test for augment-ability by trying all valid α and j , as defined above.

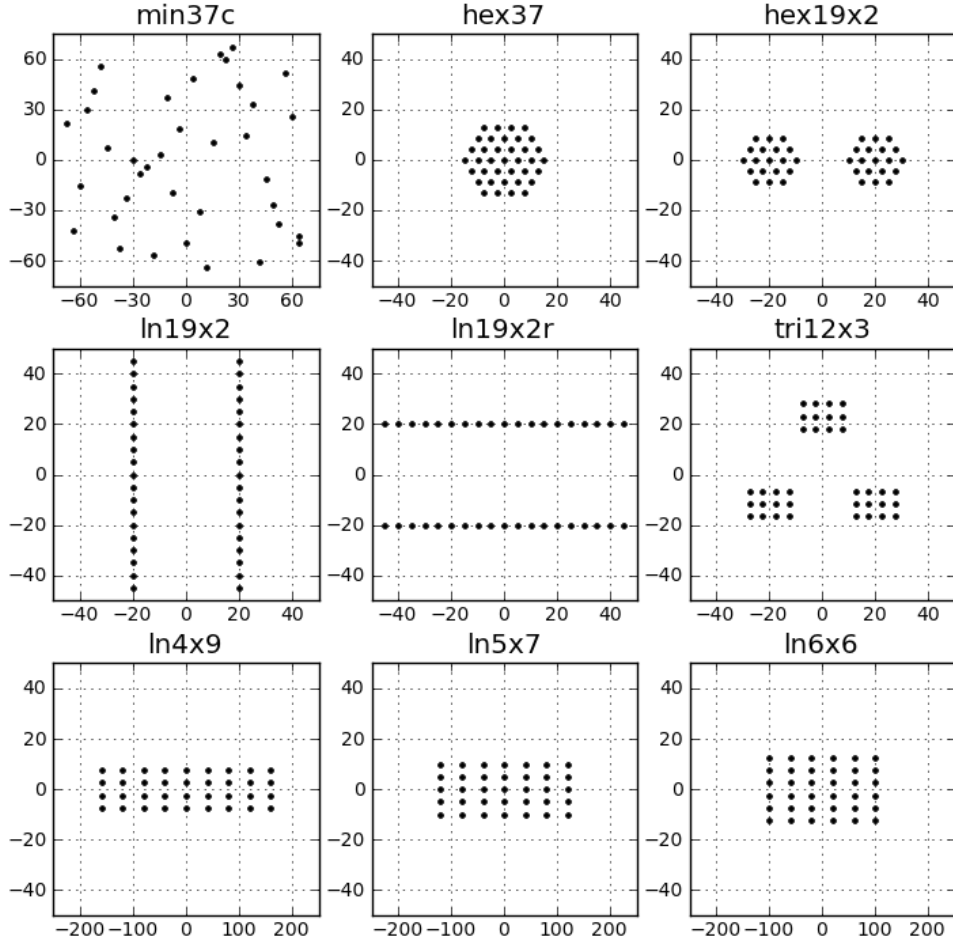


Fig. 2.— Shown above are the north-south (vertical axis) and east-west (horizontal axis) antenna positions in meters for various fiducial array configurations. With the exception of `min37c`, these arrangements aim to improve power-spectrum sensitivity in the regime where errors are not dominated by sample variance in the cosmological signal by redundantly sampling regions in the uv -plane with many baselines. The different configurations explore different design ideas, including how maximum-redundancy arrays may be generated for regions farther from the center of the uv -plane. In contrast, `min37c` (see Figure 1) is an array configuration tuned to minimize sampling redundancy, thereby improving imaging by maximizing the number of independent measurements of the uv -plane (see §3.1). The uv -sampling patterns generated by these configurations are shown in Figure 3.

Fortunately, for measuring a physical scale at reionization, a 21cm EoR experiment has considerable flexibility in choosing an angular scale, making it possible to generate antenna configurations that reap many of the sensitivity benefits of centrally-condensed configurations but which avoid some of the associated deficiencies by directing sensitivity toward higher- $|\vec{u}|$ modes. Consider, for example, a configuration consisting of two clusters of $N/2$ closely-packed antennas whose centers are separated by a distance larger than the diameter of each cluster (see **hex19x2** in Figure 2). Excluding the central region of the uv -plane sampled by intra-cluster antenna pairs, we see in Figure 3 that $N^2/4$ samples are concentrated in a region near $|\vec{u}| = 30$. In this region, excluding earth-rotation synthesis, we compute from equation B13 that $f/f_0 = N/2$. Including redundancy generated by the earth’s rotation over the course of a two-hour observation toward a transiting phase center, we compute $f/f_0 = 1.1 \times 10^4$ following equation 26. Furthermore, by adjusting the spacing between antenna clusters, this configuration can be tuned to focus sensitivity to regions of the uv -plane where galactic synchrotron and point-source foreground emission are minimized.

The **hex19x2** design described above and shown in Figure 2 can be improved upon in several ways. Firstly, perturbing the shape of antenna clusters can improve overlap resulting from earth-rotation synthesis. Long rows of antennas (see **1n19x2** in Figure 2) do well for this; as the Earth rotates, this sampling pattern slides over itself along the longest axis. As a result, the new uv -samples generated are largely redundant with regions that have already been previously sampled (see Figure 3). It should be noted that the latitude at which an array is deployed influences the design of maximum-redundancy array configurations. At latitudes near $45^\circ N/S$, the performance of the row-based configurations we explore is largely independent of the orientation of the rows. For arrays near the equator, rows oriented east-west yield better sensitivity because the spacing between rows is maintained through earth-rotation synthesis. In these cases, however, the slow fringe-rates of the north-south baselines generated may make them more susceptible to instrumental systematics. Motivated by the locations of current 21cm EoR arrays, we have restricted ourselves to considering only mid-latitudes.

An additional optimization relates to exploiting the Hermitian-symmetry of the uv -plane for a real-valued sky: a baseline vector \vec{u} also samples the uv -plane at $-\vec{u}$. As a result, for sampling the uv -plane at the location of the displacement between rows, the interior rows in antenna arrangements such as **1n4x9**, **1n5x7**, and **1n6x6** in Figure 2 are used in two pairings — once with each adjacent row. For N antennas arranged into R rows, $R - 2$ rows are used in both positive and negative pairings, generating a peak instantaneous redundancy of $N(R - 2)/R$ samples. This alone suggests that the number of rows should be maximized for best sensitivity. However, when earth-rotation synthesis is considered, the row length N/R also becomes important. By empirically comparing redundancy metrics for **1n4x9**, **1n5x7**, and **1n6x6**, and by including other comparisons for larger numbers of antennas, we have determined that the highest-redundancy configurations are generated by nearly square arrangements, with $R \approx \sqrt{N}$.

In tuning the spacing between rows, there are several competing factors that need to be considered. The first is the increasing brightness of galactic synchrotron emission at small $|\vec{u}|$

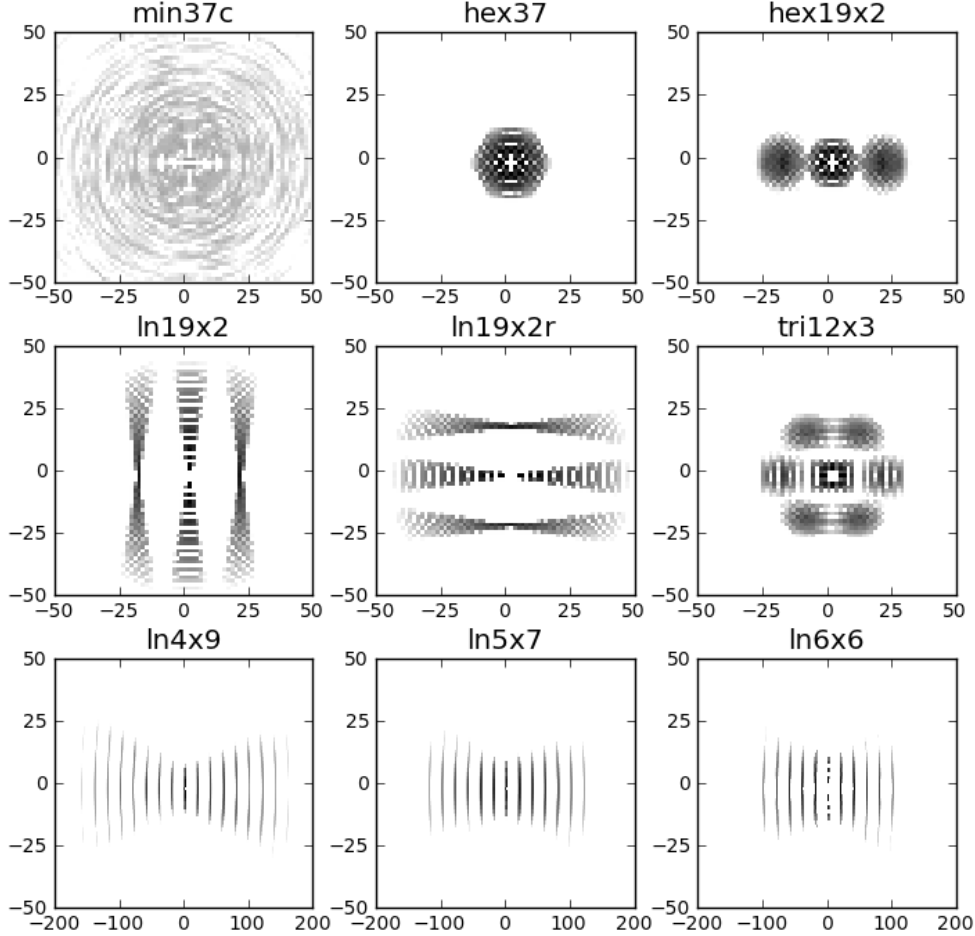


Fig. 3.— The uv -plane samplings shown above were generated for each of the antenna configurations from Figure 2, assuming a 2-hour observation at $40^\circ N$ latitude of a zenith-transiting phase center at 150 MHz. Sampling is plotted using uv -bins that are 1.5 wavelengths on a side, with color scale indicating \log_{10} of the number of one-second samples falling in each bin, ranging from 3 (white) to 5 (black). Antenna configurations generating redundant uv -sampling patterns increase sensitivity to particular Fourier modes used to probe the $\Delta_{21}^2(k)$ power spectrum at the expense of sampling multiple modes. Several of the configurations illustrated above direct sensitivity toward regions at higher $|\vec{u}|$, thereby avoiding the instrumental systematics and brighter foregrounds associated with sampling near the origin of the uv -plane. The redundancy metrics (see §2.4) computed for these sampling patterns are shown in Figure 4.

following a $C_\ell \propto \ell^{-3.7}$ scaling law (Chen 2004). Secondly, the ability to control instrumental systematics decreases with low fringe-rates. The third is that sensitivity reduces with increasing spacing owing to baselines moving more quickly through the uv -plane as the earth rotates. The fourth, which will be discussed in greater detail in a forthcoming publication, is the fact that the frequency-dependence of uv -sampling becomes increasingly problematic for foreground removal at longer baseline lengths. Finally, the increasing dominance of point-source foregrounds at higher $|\vec{u}|$ imply that there will be diminishing returns for reducing foregrounds by increasing baseline length. Taken together, these factors imply that the spacing between rows should target the shortest spacing at which galactic synchrotron emission and/or instrumental systematics do not pose a problem. To standardize the clustered antenna configurations we examine, we choose a 20-meter fiducial spacing between clusters.

Optimizing families of maximum-redundancy configuration styles is straight-forward, algorithmically. Automating a broader exploration of configuration space for maximally-redundant configurations is much more difficult, owing to the extremely low entropy of these states in configuration space. Our experience has been that random processes are highly unlikely to encounter these configurations, even when a strong selective potential is applied. In order to gain confidence that the manually-generated maximum-redundancy configurations we explore are at least nearly optimal, it is useful to compare them to the total redundancy of compact antenna configurations (see `hex37` in Figures 2 and 4). Figure 4 illustrates that in the $10 < |\vec{u}| < 20$ region for which it was optimized, the `1n5x7` configuration achieves approximately 50% of the peak redundancy of `hex37`. Hence, we may have confidence that while other configurations might outperform `1n5x7`, they will not do so by more than a factor of two.

Finally, it is worth pointing out that far from being a calibration liability, maximum-redundancy arrays may actually be more conducive to calibration than their minimum-redundancy counterparts. Redundant samplings of the uv -plane with many antenna pairings produce independent measurements of the same quantity, facilitating the calibration of per-antenna gain and phase parameters (Liu et al. 2010). Especially for configurations involving shorter baselines sensitive to large-scale structures on the sky, the fact that many baselines fundamentally measure the same quantity can improve calibration by easing the need for an accurate sky model on which to base a self-calibration loop.

3.3. Sensitivity Performance

Of the different configurations considered for maximum-redundancy arrays (see Figure 2), the optimal for sensitivity choice depends on the degree to which the shortest baselines are subject to instrumental and celestial interference. To parametrize our ignorance of what are the shortest baselines that may be effectively used, we introduce a parameter u_{\min} to describe a minimum cutoff for baselines contributing to power-spectrum sensitivity. For the antenna configurations shown in Figure 2, with corresponding uv -coverage in Figure 3, we compute the redundancy metric as a

function of u_{\min} , omitting regions inside of $|\vec{u}| < u_{\min}$ from the numerator in equation 26. The results are shown in Figure 4.

If all baselines may be used effectively to measure $\Delta_{21}^2(k)$, the most compact configuration (**hex32** in Figure 2) maximizes the redundancy metric. If baselines shorter than five wavelengths are unusable, however, the array configurations that are most effective employ rows of antennas that have high instantaneous sampling redundancy and also generate substantial redundancy through earth-rotation synthesis. In particular, we show in the bottom panel of Figure 4 that the **1n5x7** configuration dominates all other configurations within the $5 < u_{\min} < 20$ region for which its row spacing was tuned. Based on the success of this design, we extrapolate to a 132-antenna design consisting of 11 rows of 12 elements each, with a 3.75-meter spacing between antennas within a row. This configuration (labeled **1n11x12** in Figure 5) was shown to have a higher redundancy metric than 8×16 and 16×8 designs.

Using the redundancy metric read from Figure 4 at a chosen u_{\min} , we can calculate a sensitivity as a function of k by applying equation 27. In Figure 5, we plot the sensitivities for selected configurations using observation parameters matched to the PAPER experiment operating at 150 MHz with a 6-MHz observing bandwidth, assuming 120-day drift-scan observations over six sidereal hours of sky using phase centers spaced two hours apart. We compare these sensitivities with a toy reionization model derived from equation 21 under optimistic assumptions that produce 100 mK^2 peak fluctuations in the range $0.1 < k < 10h \text{ Mpc}^{-1}$. As shown in Figure 5, we find that a 132-antenna deployment of PAPER antennas will, under ideal conditions, have the requisite sensitivity to detect peak 21cm EoR fluctuations at a 3σ level at $k < 0.25h \text{ Mpc}^{-1}$ with approximately four months of observation. This result is contingent upon antennas being deployed in a maximum-redundancy configurations, and does not include the potential effects of foreground removal on sensitivity, which will be discussed in a future paper. As shown by the sensitivity curves for minimum-redundancy configurations (**min37** and **min37c** in Figure 5), maximum-redundancy configurations yield nearly an order-of-magnitude improvement in sensitivity for 37-antenna arrays. This improvement is larger for bigger arrays, owing to the fact that $f/f_0 \propto N^2$ for maximum-redundancy arrays, whereas $f/f_0 = 1$ for minimum-redundancy arrays (except when scaling configurations below the critical size where adjacent samples of the uv -plane are no longer independent; in this case, redundancy scales with maximum baseline length as $f/f_0 \propto u_{\max}^{-4}$).

Although these sensitivity figures were computed using observing parameters for the PAPER experiment, it is straightforward to extrapolate them to other experiments. In particular, equation 27 makes very few assumptions about observing strategies that may differ between experiments — all such differences are grouped into the numerically computed redundancy factor. PAPER employs drift-scan observations that limit observing time toward one phase center to approximately two hours. For experiments that track the sky with dishes or with station beam-forming, the amount of time spent observing toward the same phase center may be considerably longer. As a result, there may be additional redundancy generated by using earth-rotation synthesis over longer periods. In all of these cases, computing the sampling generated for a single phase center yields the correct

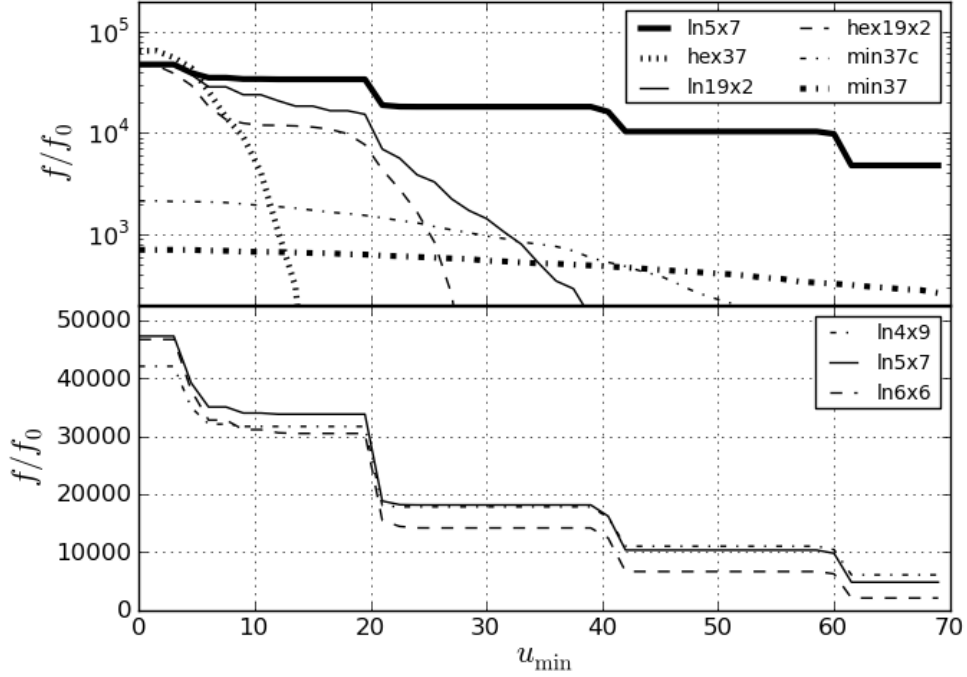


Fig. 4.— Plotted above is the redundancy metric f/f_0 (relating to sensitivity, see Eq. 26) for several of the antenna configurations in Figure 2 as a function of the minimum distance u_{\min} that may be used for power-spectrum analysis, owing to bright foreground emission and instrumental systematics associated with low fringe rates (see §3.3). The most centrally condensed configuration (**hex37**) maximizes f if regions within u_{\min} are not omitted. If a region with radius $u_{\min} > 5$ wavelengths is omitted, configurations with larger separations are preferable, most notably **ln5x7**, which dominates all other configurations out to twice the separation between antenna rows. For comparison, two minimum-redundancy configurations (**min37** and **min37c**, see Figure 1) are also plotted. The lower plot highlights how the number of rows in a configuration affects redundancy.

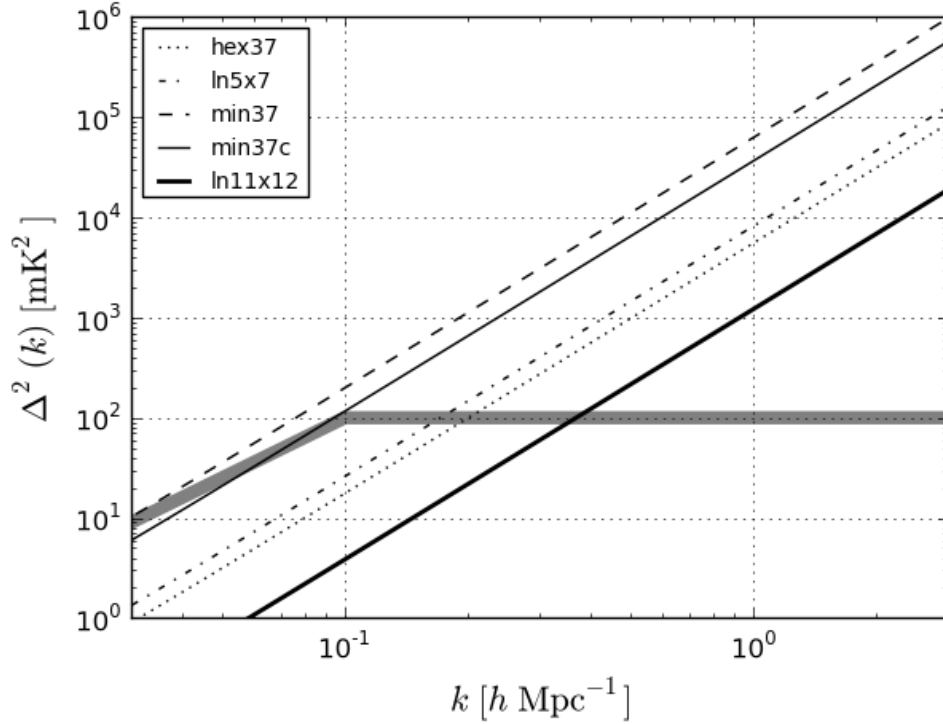


Fig. 5.— This plot shows ideal, 1σ noise-sensitivity levels to the 21cm EoR power spectrum using various array configurations at 150 MHz, assuming PAPER observing parameters for 120-day drift-scan observations over six sidereal hours of sky with a 6-MHz observing bandwidth (see equation 27). Except for **hex37** (where $u_{\min} = 0$ is used), the sensitivities shown assume $u_{\min} = 10$ from Figure 4. Minimum-redundancy configurations (**min37** and **min37c**, above) show significantly reduced sensitivity relative to the best-performing **ln5x7** maximum-redundancy configuration. The **ln11x12** configuration is an extension of the **ln5x7** design to 132 antennas, with a 3.75-meter pitch between antennas within a row. The thick black line denotes an optimistic toy model for peak 21cm EoR fluctuations (see equation 21). Predictions for the signal range between this curve and a factor of ten smaller. In this plot, k is dominated by the line-of-sight component for the compact configurations we consider; at smaller k , sensitivity departs from a power-law as the contribution of a baseline’s length to k becomes important.

redundancy value for use in equation 27.

A natural question that arises from the efficacy of antenna clustering for improving sensitivity is whether, given the density of sampling within a row, it might be desirable to employ larger antenna elements (perhaps parabolic cylinders) in lieu of numerous smaller antenna elements. Phrased differently, is the $\mathcal{O}(N)$ improvement to SNR that results from implementing a fixed collecting area with N antenna elements worth the $\mathcal{O}(N^2)$ cost of correlating them? In the limit that the correlator is a dominant cost in the construction of an array, using large dishes, beam-forming antennas prior to correlation, or even operating separate sub-arrays may all represent attractive options for more cheaply improving sensitivity. On the other hand, extrapolating from currently deployed systems using Moore’s Law applied to computational density suggests correlators might not be the dominant cost for forthcoming arrays (Jason Manley, personal communication), in which case smaller elements yield the best sensitivity for a fixed collecting area. This case may be even stronger, noting that array configurations consisting of parallel rows are particularly conducive to correlation via electric-field gridding techniques (Tegmark & Zaldarriaga 2009) that replace the $\mathcal{O}(N^2)$ scaling of the computational cost of correlators with an $\mathcal{O}(N \log N)$ scaling based on the fast Fourier transform algorithm.

4. Conclusion

Reionization experiments aiming to detect the power spectrum of 21cm EoR fluctuations will need to achieve a tremendous level of foreground removal. For characterizing these foregrounds, minimum-redundancy array configurations are most useful. However, as efforts turn to constraining the three-dimensional power spectrum of 21cm EoR fluctuations, the maximum-redundancy configurations we have presented provide a substantial increase in sensitivity over their minimum-redundancy counterparts in the regime where sensitivity is not limited by sample variance in the cosmological signal — a regime that 21cm reionization arrays will find themselves in for the foreseeable future. While the most compact antenna arrangements yield the highest-redundancy sampling of the uv -plane, the performance of these arrangements may be compromised by increased foreground brightness at low $|\vec{u}|$ and by instrumental systematics associated with low fringe-rates.

In order to avoid the difficulties of working near the origin of the uv -plane, we show how maximum-redundancy array configurations can be tuned to regions of the uv -plane where foregrounds and systematics are likely to be smaller. Of particular interest are a class of configurations using parallel rows of antennas that generate substantial instantaneous sampling redundancy, but are also aligned to enhance redundancy through earth-rotation synthesis. Using such a configuration, we demonstrate that under ideal conditions, a 132-antenna deployment of PAPER observing for 120 days will have the requisite sensitivity to detect the power spectrum of the brightest expected reionization fluctuations at a 3σ level at $k < 0.25h \text{ Mpc}^{-1}$, using bins of $\Delta \ln k = 1$. The real-world sensitivity of such an array will be affected by foreground removal requirements and actual performance, and could be worse than this.

Next-generation 21cm reionization arrays such as phase-II of HERA will have improved sensitivity. Even so, HERA’s choice of array configuration must balance the competing goals of imaging bright EoR structures and characterizing the power-spectrum of EoR fluctuations. For current and future arrays, this choice must be informed by parameters that are currently poorly constrained: the degree to which foregrounds can be modeled, removed, or otherwise differentiated from the 21cm EoR signal; the angular power spectra of the dominant foregrounds; the nature of instrumental systematics that arise; and the geometry and collecting area of the most effective antenna elements. Exploration of these design parameters is underway with phase-I HERA efforts such as PAPER and the MWA. PAPER is in a unique position to use the mobility of its antennas to explore different configurations for 21cm reionization work. Maximum-redundancy arrays can be used to push sensitivity limits for power-spectrum measurements while minimum-redundancy configurations will help glean more information about foreground properties. Near-term activities can explore the results of tuning array sensitivity relative to foreground brightness and examine the influence of cross-coupling and crosstalk on power-spectrum measurements. Continued work in this area will aim to establish an optimal array design for next-generation 21cm EoR work.

Acknowledgement

We dedicate this paper to the memory of Don Backer, who pioneered PAPER and laid the foundations for HERA. AP thanks Philip Matchett Wood for helpful discussions of Golomb rulers and Costas arrays and acknowledges support from the NSF AAPF (#0901961) and from the Charles H. Townes Postdoctoral Fellowship. MM acknowledges support from the Einstein Postdoctoral Fellowship. PAPER is supported through the NSF-AST program (#0804508).

A. Sensitivity from Combining Independent \vec{k} -modes

This appendix derives equation 25 in full. We treat each of the three sources of independent samples mentioned in §2.3 separately. We begin with equation 20, reproduced here:

$$\Delta_N^2(k) \approx 2.8 \times 10^4 \left[\frac{k}{0.1h \text{ Mpc}^{-1}} \right]^3 \left[\frac{\Omega}{0.76 \text{ sr}} \right]^{\frac{3}{2}} \times \left[\frac{T_{\text{sys}}}{500 \text{ K}} \right]^2 \left[\frac{120 \text{ days}}{t_{\text{days}}} \right] \left[\frac{|\vec{u}|}{20} \right] \text{ mK}^2. \tag{A1}$$

A.1. Combining Modes Along the Line-of-Sight

Let us bin the line-of-sight modes in logarithmic increments. For a fixed logarithmic bin size of $\Delta \ln k$, the number of modes in each bin grows linearly with k and linearly with the chosen

observing bandwidth B . The bandwidth term enters because it sets the total number of k -modes measured for a constant frequency channel resolution. We incorporate these scalings into equation A1, using that sensitivity will scale as the square-root of the number of independent \vec{k} -modes binned, and counting the modes in a fiducial bin to set the prefactor. For a bin centered around $k = 0.1h \text{ Mpc}^{-1}$, a bin of width $\Delta \ln k$ has bin edges at $0.06h$ and $0.165h \text{ Mpc}^{-1}$. A bandwidth of 6MHz produces a \vec{k} -space resolution of $2\pi/YB \approx 0.083h \text{ Mpc}^{-1}$, where Y is given by equation 18. Therefore, we count approximately 1.27 independent \vec{k} -modes, resulting in a $\sqrt{1.27} \approx 1.13$ -fold increase in sensitivity, or

$$\begin{aligned} \Delta_{\text{N}}^2(k) \approx & 2.48 \times 10^4 \left[\frac{k}{0.1h \text{ Mpc}^{-1}} \right]^{\frac{5}{2}} \left[\frac{6 \text{ MHz}}{B} \right]^{\frac{1}{2}} \left[\frac{1}{\Delta \ln k} \right]^{\frac{1}{2}} \\ & \times \left[\frac{\Omega}{0.76 \text{ sr}} \right]^{\frac{3}{2}} \left[\frac{T_{\text{sys}}}{500 \text{ K}} \right]^2 \left[\frac{120 \text{ days}}{t_{\text{days}}} \right] \left[\frac{|\vec{u}|}{20} \right] \text{ mK}^2. \end{aligned} \quad (\text{A2})$$

A.2. Combining Time Samples and Modes Across the uv -plane

To combine modes measured by different baselines throughout the uv -plane and to calculate the amount of time a baseline samples a single (u, v, η) mode, we must assume an array configuration. As stated in §2.3, we assume an array configuration that generates uniform, non-overlapping coverage in the uv -plane out to a radius u_{max} . This assumption makes the problem algebraically tractable, and is similar to the minimum-redundancy arrays discussed in §3.1. We explicitly sum measurements from (u, v, η) -mode bins, or “ uv -pixels”, over the uv -plane. We use the calculated the noise in any uv -pixel from equation A2, and add up all the samples within each ring of constant uv -distance $|\vec{u}|$. Finally, we sum over all the rings out to u_{max} .

Let us define two additional terms. Let the sampling density of the uv -plane, ρ , be given by

$$\rho \equiv \frac{N_{\text{bl}}}{\pi u_{\text{max}}^2} \approx \frac{N^2}{2\pi u_{\text{max}}^2}, \quad (\text{A3})$$

where N_{bl} is the number of baselines and N is the number of antenna elements. This equation restates our assumption that the uv -plane is uniformly sampled out to a radius u_{max} . We also define $t_{\text{per_mode}}$, the time a baseline samples a single uv -pixel relative to a chosen phase center before earth rotation moves it into another pixel:

$$t_{\text{per_mode}} \equiv t_{20} \left[\frac{\Omega_0}{\Omega} \right]^{\frac{1}{2}} \left[\frac{20}{|\vec{u}|} \right], \quad (\text{A4})$$

where t_{20} is the amount of time a 20-wavelength baseline spends in one pixel (used a fiducial scale), Ω_0 is a fiducial primary beam size (0.76 sr for PAPER), and $|\vec{u}|$ is the baseline length. Note that, per the assumptions of the derivation in §2.3, we neglect here the possibility that multiple baselines may sample the same uv -pixel under earth-rotation synthesis. Note also that t_{20} depends on the

array latitude; for PAPER it is approximately 13 minutes; this factor has already been absorbed into the prefactor in equation 20.

With these terms defined, we first calculate the number of uv -pixels within a ring of radius u . We choose an arbitrary ring width w , which will drop out of the derivation later. The number of baselines that sample within this ring is then:

$$N_{\text{bl}} \approx 2\pi|\vec{u}|w\rho. \quad (\text{A5})$$

The number of pixels sampled depends on the observing time, $t_{\text{per_day}}$ and the time spent in each pixel, $t_{\text{per_mode}}$:

$$N_{\text{px,ring}} = N_{\text{bl}} \left[\frac{t_{\text{per_day}}}{t_{\text{per_mode}}} \right]. \quad (\text{A6})$$

To calculate the sensitivity of one ring in the uv -plane, we average over the sensitivity of each pixel within the ring. Each pixel within the ring has equal sensitivity (e.g. equation A2), so this is a simple, unweighted average:

$$\Delta_{\text{N,ring}}^2 = \frac{\sum_{\text{px}} \Delta_{\text{N,px}}^2}{N_{\text{px}}} = \frac{\Delta_{\text{N,px}}^2}{\sqrt{N_{\text{px}}}}, \quad (\text{A7})$$

where $\Delta_{\text{N,px}}^2$ is given by equation A2. Plugging in values calculated above gives:

$$\Delta_{\text{N,ring}}^2 = \frac{\Delta_{\text{N,px}}^2}{\sqrt{2\pi|\vec{u}|w\rho \frac{t_{\text{per_day}}}{t_{\text{per_mode}}}}} = \frac{\Delta_{\text{N,px}}^2}{\sqrt{2\pi|\vec{u}|w\rho \frac{t_{\text{per_day}}}{t_{20}} \left[\frac{\Omega}{\Omega_0} \right]^{\frac{1}{2}} \frac{|\vec{u}|}{20}}}. \quad (\text{A8})$$

The next step is to combine all the measurements from different rings. In the case presented here, the noise power in each ring is equal, as the $\sqrt{|\vec{u}|^2}$ term in the denominator of equation A8 cancels the $|\vec{u}|$ term in equation A2. We can therefore do another unweighted average to combine the rings:

$$\Delta_{\text{N}}^2 = \frac{\sum_{\text{rings}} \Delta_{\text{N,ring}}^2}{N_{\text{rings}}} = \frac{\Delta_{\text{N,ring}}^2}{\sqrt{N_{\text{rings}}}} = \frac{\Delta_{\text{N,ring}}^2}{\sqrt{u_{\text{max}}/w}}, \quad (\text{A9})$$

where the last step uses the fact that the number of rings is the radius of the circle over the width of a ring, u_{max}/w . Plugging equations A2 and A3 into this equation yields:

$$\Delta_{\text{N}}^2 = \Delta_{\text{N,px}}^2 \left[\frac{20}{|\vec{u}|} \right] \left[\frac{\Omega_0}{\Omega} \right]^{\frac{1}{4}} \left[\frac{t_{20}}{t_{\text{per_day}}} \right]^{\frac{1}{2}} \left[\frac{u_{\text{max}}}{20} \right]^{\frac{1}{2}} \left[\frac{1}{N} \right]. \quad (\text{A10})$$

We then reach our final result by substituting in equation A8, choosing a fiducial observation time

of $t_{\text{per.day}} = 6$ hours (recall that $t_{20} \approx 13\text{min}$), and choosing an array size of $N = 32$ elements:

$$\begin{aligned} \Delta_{\text{N}}^2(k) &\approx 150 \left[\frac{k}{0.1h \text{ Mpc}^{-1}} \right]^{\frac{5}{2}} \left[\frac{6 \text{ MHz}}{B} \right]^{\frac{1}{2}} \left[\frac{1}{\Delta \ln k} \right]^{\frac{1}{2}} \\ &\times \left[\frac{\Omega}{0.76 \text{ sr}} \right]^{\frac{5}{4}} \left[\frac{T_{\text{sys}}}{500 \text{ K}} \right]^2 \left[\frac{6 \text{ hrs}}{t_{\text{per.day}}} \right]^{\frac{1}{2}} \\ &\times \left[\frac{120 \text{ days}}{t_{\text{days}}} \right] \left[\frac{u_{\text{max}}}{20} \right]^{\frac{1}{2}} \left[\frac{32}{N} \right] \text{ mK}^2. \end{aligned} \quad (\text{A11})$$

B. Sensitivity from Combining Redundant Samples of \vec{k} -modes

In this appendix, we first motivate our definition of the redundancy factor presented in equation 26 in B.1. Next, in B.2 we derive equation 27 in full. Finally, we present an analytic calculation of the redundancy metric for a filled circular aperture in B.3.

Several times below we will refer to sensitivity relative to a fiducial measurement. For this benchmark, we choose a single baseline with a one-second integration, which we call $\Delta_{\text{N},1\text{sec}}^2$. The choice of fiducial integration time is arbitrary, but affects the scaling constants in the equations that follow. For baselines with length $|\vec{u}| < 10^4$ (essentially all baselines useful for EoR measurements), earth-rotation is unimportant on one-second timescales. Therefore, our fiducial measurement is equal to equation 16,

$$\Delta_{\text{N},1\text{sec}}^2(k) \equiv X^2 Y \frac{k^3}{2\pi^2} \frac{\Omega}{2t} T_{\text{sys}}^2, \quad (\text{B1})$$

with $t = 1$ second.

B.1. Motivation for the Redundancy Metric

In this section, we outline a formalism for computing the sensitivity of a generic antenna array, expressed in terms of a redundancy metric. The sensitivity calculation in §2.3 and Appendix A assumed a uv -coverage that produces equal sensitivity in any ring of the uv -plane. We were then able to perform an unweighted average to get the final sensitivity by summing over rings. More generally, the final sensitivity will be a weighted average of the sensitivity of all the uv -pixels:

$$\Delta_{\text{N}}^2 = \frac{\sum_i w_i \Delta_{\text{N},i}^2}{\sum_i w_i}, \quad (\text{B2})$$

where i is an index labeling an individual uv -pixel and $\Delta_{\text{N},i}^2$ is the noise variance of a mode. The optimal weights for any pixel are proportional to the inverse variance of noise in that pixel. Since repeated measurements of a uv -pixel add coherently in temperature, redundant measurements beat

down the noise in temperature-squared *linearly* with the number of samples. Therefore, we choose optimal inverse-variance weights $w_i = n_i^2$, where n_i is the number of fiducial samples in that pixel, and equation B2 then becomes:

$$\Delta_N^2 = \frac{\sum_i n_i^2 \frac{\Delta_{N,1\text{sec}}^2}{n_i}}{\sum_i n_i^2} = \frac{\sum_i n_i \Delta_{N,1\text{sec}}^2}{\sum_i n_i^2} \quad (\text{B3})$$

We further simplify this equation by noting that the coefficients of a weighted sum of random numbers will add in quadrature:

$$\Delta_N^2 = \frac{\sqrt{\sum_i n_i^2 \Delta_{N,1\text{sec}}^4}}{\sum_i n_i^2} = \frac{\Delta_{N,1\text{sec}}^2}{\sqrt{\sum_i n_i^2}}, \quad (\text{B4})$$

We compare this result to the reduction in noise that would occur without any two samples being of the same mode (i.e. n_i being uniformly unity):

$$\Delta_{N,\text{no-red}}^2 = \frac{\sqrt{\sum_j \Delta_{N,1\text{sec}}^4}}{\sum_j 1} = \frac{\Delta_{N,1\text{sec}}^2}{\sqrt{\sum_j 1}} \quad (\text{B5})$$

where the index j labels pixels. (We use a different letter here to differentiate these modes from those used in equation B4). The number of samples has remained constant between this case and the one calculated above, $\sum_j 1 = \sum_i n_i$, giving us:

$$\Delta_{N,\text{no-red}}^2 = \frac{\Delta_{N,1\text{sec}}^2}{\sqrt{\sum_i n_i}} \quad (\text{B6})$$

The relative improvement of redundant sampling over the completely non-redundant case is the ratio between these two terms:

$$\frac{\Delta_N^2}{\Delta_{N,\text{no-red}}^2} = \frac{\Delta_{N,1\text{sec}}^2 \sqrt{\sum_i n_i}}{\sqrt{\sum_i n_i^2} \Delta_{N,1\text{sec}}^2} = \sqrt{\frac{\sum_i n_i}{\sum_i n_i^2}} \quad (\text{B7})$$

We use this result to motivate the definition of our metric for the sampling redundancy given in equation 26:

$$\frac{f}{f_0} \equiv \frac{\sum_i n_i^2}{\sum_i n_i}. \quad (\text{B8})$$

B.2. Derivation of Maximum-Redundancy Sensitivity

To derive array sensitivity including the effects of sampling redundancy, we begin by evaluating equation B1 at $z = 9$, substituting in equation 19:

$$\Delta_{\text{N},1\text{sec}}^2(k) \approx \frac{540.}{4\pi^2} k^3 \Omega T_{\text{sys}}^2 \frac{h^{-3} \text{Mpc}^3}{\text{sr Hz s}}. \quad (\text{B9})$$

Expressing the result in terms of our fiducial observing and telescope parameters gives:

$$\Delta_{\text{N},1\text{sec}}^2(k) \approx 2.6 \times 10^9 \left[\frac{k}{0.1h \text{ Mpc}^{-1}} \right]^3 \left[\frac{\Omega}{0.76 \text{ sr}} \right]^{\frac{3}{2}} \left[\frac{T_{\text{sys}}}{500 \text{ K}} \right]^2 \text{mK}^2. \quad (\text{B10})$$

Next, we incorporate several sensitivity contributions calculated previously: a factor of 1.13 for logarithmic binning of line-of-sight modes (derived in Appendix A.1), a factor of $(2.16 \times 10^4)^{\frac{1}{2}}$ for the number of independent 1-second observations in a 6-hour observing window, and a factor of 120 for the number of days observed. There is also a factor of $(N_{\text{baselines}})^{\frac{1}{2}}$ sensitivity increase, since each baseline provides an independent sample at every integration. For our fiducial array of 32 antennas, this term is $\approx \sqrt{512}$. The result is an expression for the sensitivity of an array, assuming that every integration of every baseline is treated as a sample of an independent \vec{k} -mode:

$$\begin{aligned} \Delta_{\text{N}}^2(k) &\approx 5.8 \times 10^3 \left[\frac{k}{0.1h \text{ Mpc}^{-1}} \right]^{\frac{5}{2}} \left[\frac{6 \text{ MHz}}{B} \right]^{\frac{1}{2}} \left[\frac{1}{\Delta \ln k} \right]^{\frac{1}{2}} \\ &\times \left[\frac{\Omega}{0.76 \text{ sr}} \right]^{\frac{3}{2}} \left[\frac{T_{\text{sys}}}{500 \text{ K}} \right]^2 \left[\frac{6 \text{ hrs}}{t_{\text{per.day}}} \right]^{\frac{1}{2}} \left[\frac{120 \text{ days}}{t_{\text{days}}} \right] \text{mK}^2. \end{aligned} \quad (\text{B11})$$

Finally, as derived in Appendix B.1, the effects of sampling redundancy may be included by introducing a factor of $[f/f_0]^{\frac{1}{2}}$. Using a fiducial value of $f/f_0 = 10^4$, we have our final result:

$$\begin{aligned} \Delta_{\text{N}}^2(k) &\approx 58 \left[\frac{k}{0.1h \text{ Mpc}^{-1}} \right]^{\frac{5}{2}} \left[\frac{6 \text{ MHz}}{B} \right]^{\frac{1}{2}} \left[\frac{1}{\Delta \ln k} \right]^{\frac{1}{2}} \\ &\times \left[\frac{\Omega}{0.76 \text{ str}} \right] \left[\frac{T_{\text{sys}}}{500 \text{ K}} \right]^2 \left[\frac{6 \text{ hrs}}{t_{\text{per.day}}} \right]^{\frac{1}{2}} \\ &\times \left[\frac{120 \text{ days}}{t} \right] \left[\frac{32}{N} \right] \left[\frac{10^4 f_0}{f} \right]^{\frac{1}{2}} \text{mK}^2. \end{aligned} \quad (\text{B12})$$

B.3. Calculating f/f_0 for a Filled Circular Aperture

Here we explicitly calculate the instantaneous redundancy of an array where antennas are arranged to uniformly sample an aperture within a region defined by $|\vec{r}| < R$, with zero sampling elsewhere. Using that the convolution of two disks of area πR^2 is a cone of height $h = \pi R^2$ and

base radius $2R$, we can compute:

$$\begin{aligned}
 f &= \frac{\int_0^{2R} 2\pi r \, dr \, h^2 \left(1 - \frac{r}{2R}\right)^2}{\int_0^{2R} 2\pi r \, dr \, h \left(1 - \frac{r}{2R}\right)} \\
 &= \frac{2\pi h^2 \left(\frac{r^2}{2} - 2\frac{r^3}{6R} + \frac{r^4}{16R^2}\right) \Big|_0^{2R}}{2\pi h \left(\frac{r^2}{2} - \frac{r^3}{6R}\right) \Big|_0^{2R}} = \frac{h}{2}
 \end{aligned}
 \tag{B13}$$

Using that $h = \pi R^2 = NA_e$, where N is the number of antennas and A_e is the effective area of a single antenna, we have $f = NA_e/2 = Nf_0$. In general, the redundancy metric must be calculated numerically to account for more complicated array configurations and the effects of earth-rotation synthesis.

REFERENCES

- Babcock, W. 1953, Bell System Technical Journal, 31, 63
- Bernardi, G., et al. 2010, A&A, 522, A67+
- Bowman, J., et al. 2006, ApJ, 638, 20
- . 2009, ApJ, 695, 183
- Bowman, J. & Rogers, A. 2010, Nature, 468, 796
- Chen, X. 2004, arXiv:astro-ph/0409733
- Clark, B. 1999, in ASP Conf. Series, Vol. 180, Synth. Imaging in Radio Ast. II, ed. Taylor, Carilli, & Perley, 1–+
- Comm. for a Decadal Survey of A&A; NRC. 2010, New Worlds, New Horizons in A&A (Natl. Acad. Press)
- Cornwell, T., et al. 2003, W-Projection: A New Algorithm for Non-Coplanar Baselines, EVLA Memo 67
- Costas, J. 1984, in Proc. of the IEEE, Vol. 72, 996–1009
- de Villiers, M. 2007, A&A, 469, 793
- Field, G. 1958, Proc. IRE, 46, 240
- Furlanetto, S., et al. 2006, Phys. Rep., 433, 181
- Golomb, S. & Taylor, H. 1984, Proc. of the IEEE, 72, 1143

- Golomb, S. & Gong, G. 2004, *Signal Design for Good Correlation: For Wireless Comm., Crypt., and Radar* (NY, NY: Cambridge Univ. Press)
- Jelić, V., et al. 2008, *MNRAS*, 389, 1319
- Keto, E. 1997, *ApJ*, 475, 843
- Lidz, A., et al. 2008, *ApJ*, 680, 962
- Liu, A., et al. 2010, *MNRAS*, 408, 1029
- Lonsdale, C., et al. 2009, *Proc. of the IEEE*, 97, 1497
- Madau, P., et al. 1997, *ApJ*, 475, 429
- McQuinn, M., et al. 2007, *MNRAS*, 377, 1043
- McQuinn, M., et al. 2006, *ApJ*, 653, 815
- Morales, M. 2005, *ApJ*, 619, 678
- Morales, M. & Hewitt, J. 2004, *ApJ*, 615, 7
- Paciga, G., et al. 2010, *ArXiv*: 1006.1351
- Park, C., et al. 2003, *ApJ*, 589, 67
- Parsons, A., et al. 2010, *AJ*, 139, 1468
- Pen, U., et al. 2009, *MNRAS*, 399, 181
- Petrovic, N. & Oh, S. 2010, *ArXiv*: 1010.4109
- Robinson, J. 1985, *IEEE Trans. on Information Theory*, 31, 781
- Rottgering, H., et al. 2006, *arXiv:astro-ph/0610596*
- Santos, M., et al. 2005, *ApJ*, 625, 575
- Sidon, S. 1932, *Mathematische Annalen*, 106, 536
- Tegmark, M. & Zaldarriaga, M. 2009, *Phys. Rev. D*, 79, 083530
- Thompson, A. 1999, in *ASP Conf. Series*, Vol. 180, *Synth. Imaging in Radio Ast. II*, ed. Taylor, Carilli, & Perley, 11–+
- Trac, H. & Cen, R. 2007, *ApJ*, 671, 1
- Wrobel, J. & Walker, R. 1999, in *ASP Conf. Series*, Vol. 180, *Synth. Imaging in Radio Ast. II*, ed. Taylor, Carilli, & Perley, 171–+

Zahn, O., et al. 2007, ApJ, 654, 12